Electronic Supporting Information

for

Probing fundamental losses in nanostructured Ta_3N_5 photoanodes: design principles for efficient water oxidation

Vikas Nandal,[*a‡] Yuriy Pihosh,[*b‡] Tomohiro Higashi,[c] Tsutomu Minegishi,[d] Taro Yamada,[b] Kazuhiko Seki, [*a] Masakazu Sugiyama,[d] and Kazunari Domen[*b]

[a] *Nanomaterials Research Institute, National Institute of Advanced Industrial Science and Technology, 1-1-1 Higashi, Tsukuba, Ibaraki 305-8565, Japan*

[b] *University Professors Office, The University of Tokyo, 7-3-1 Hongo, Bunkyo-ku, Tokyo 113-8656, Japan*

[c] *Department of Chemical System Engineering, School of Engineering, The University of Tokyo, 7-3-1 Hongo, Bunkyo-ku, Tokyo 113-8656, Japan*

[d] *Research Center for Advanced Science and Technology, The University of Tokyo, 4-6-1, Komaba, Meguro-ku, Tokyo 153-8904, Japan.*

** Email: nk.nandal@aist.go.jp, pihosh_y@arpchem.t.u-tokyo.ac.jp, k-seki@aist.go.jp,*

domen@chemsys.t.u-tpkyo.ac.jp,

‡ Authors with equal contribution.

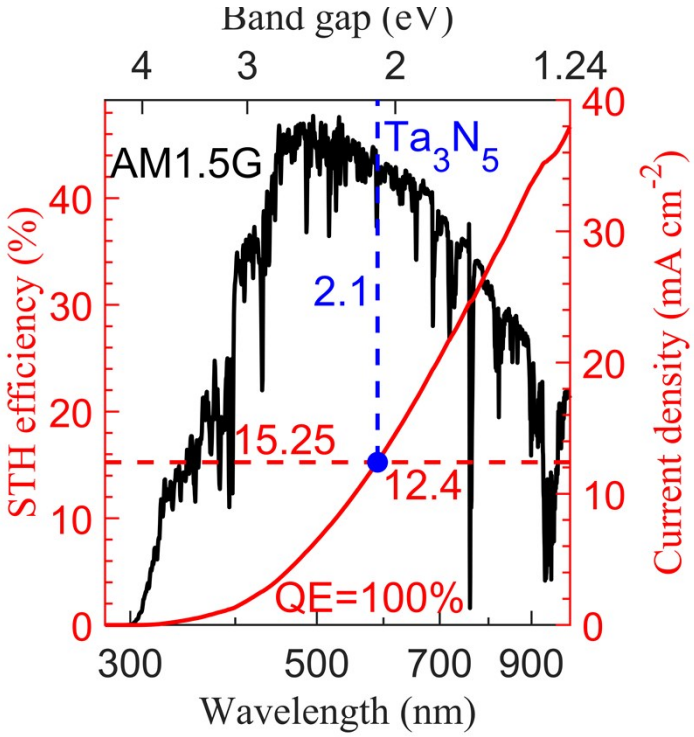

Fig. S1. Maximum theoretical solar-to-hydrogen (STH) efficiency and current density values obtained for Ta_3N_5 under AM1.5G solar illumination at 100 mW cm^{-2}. Using a Ta_3N_5 band gap of 2.1 eV and 100% external quantum efficiency (QE), the calculated STH efficiency and current density were 15.25% and 12.4 mA cm^{-2}, respectively.

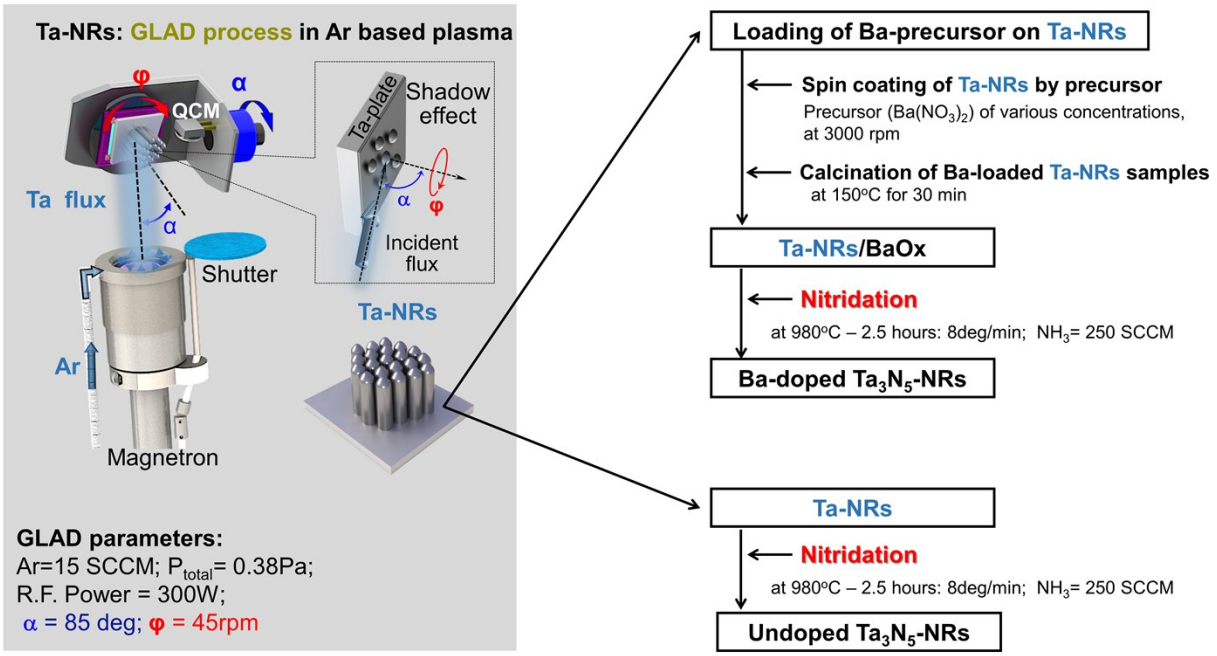

Fig. S2. Schematic illustration of the fabrication of Ba-doped Ta_3N_5-nanorods (Ba:Ta_3N_5-NRs) and undoped Ta_3N_5-NRs on a Ta substrate employing the glancing angle deposition (GLAD) and spin coating techniques followed by nitridation.

GLAD process for the preparation of NRs As shown in Fig. S2, as Ta-NRs were prepared using a custom-built GLAD system comprising a magnetron sputtering source and a three dimensional rotating platform. The platform could be adjusted to give a range of positions and glancing angle values, α. Turbomolecular pumps were employed to create a base pressure of 6×10^{-4} Pa in the GLAD system. A Ta target (99.99%, Furuchi Chem. Co) was sputtered using a magnetron source in conjunction with an Ar gas flow rate of 15 sccm at a working pressure of 0.38 Pa to produce a Ta flux that was directed towards a Ta substrate (10 × 10 × 0.3 mm, 99.95%, Nilaco Co., mirror polished) on the rotating platform, with an α of 85°. Pre-sputtering was performed with the magnetron shutter closed for 15 min at a radio frequency power of 300 W. After achieving a constant deposition rate of the sputtered Ta material, the GLAD process was initiated with the Ta substrate rotated at a rate, ϕ, of 45 rpm. As a result of the shadowing effect and the limited diffusion of adatoms,[1–4] the deposited film had a columnar structure made of well separated, vertically aligned Ta-NRs that uniformly covered the Ta substrate.

Fabrication of Ba-doped and undoped Ta_3N_5-NRs Fig. S2 summarizes the process employed to prepare Ba-doped Ta_3N_5-NRs (Ba:Ta_3N_5-NRs) and undoped Ta_3N_5-NRs from Ta/Ta-NRs samples. The Ba:Ta_3N_5-NRs

were obtained by initial loading with a Ba precursor using a spin coating method. Ba precursor solutions with concentrations of 0.025, 0.05, 0.125, 0.15 or 1 M were prepared by dissolving barium nitrate (($Ba(NO_3)_2$; 99.999%, Sigma-Aldrich) in Milli-Q water. During the loading process, the Ta/Ta-NRs samples were first wetted with a few drops of the $Ba(NO_3)_2$ solution and then left to sit for approximately 2 min, after which they were rotated at 3000 rpm for 1 min using a spin coater (model N100S, Asumi Giken, Japan). Each specimen was subsequently calcined by heating on a 150 °C hot plate in air for 30 min to obtain Ta-NRs/BaO_x specimens. Both Ba:Ta_3N_5-NRs and Ta_3N_5-NRs were then fabricated based on nitridation of the Ta-NRs/BaO_x and Ta-NRs, respectively. Nitridation was carried out by placing the respective samples in an alumina boat situated within a quartz tube connected to gas lines by air-tight flanges. The quartz tube was then purged with nitrogen (N_2) gas at a flow rate of 250 sccm for approximately 20 min, after which gaseous ammonia (NH_3) was introduced at 250 sccm for 10 min. The samples were subsequently heated at a temperature ramp of approximately 8 °C min^{-1} to 980 °C and held at that temperature for 2.5 h, followed by natural cooling to ambient temperature while continuing the same flow rate of NH_3. When the temperature in the nitridation furnace dropped to 25 °C, the flow of NH_3 gas was stopped and N_2 gas was introduced again at 250 sccm for approximately 15 min to remove residual NH_3 before removing the specimen.

Structural and morphological characterizations of the photoanodes X-ray diffraction (XRD) patterns (Smart Lab, Rigaku, Japan) were obtained using CuK_a radiation to determine the crystal structures and degrees of crystallinity of the Ta_3N_5-NRs and Ba:Ta_3N_5-NRs photoanodes. Scanning electron microscopy (SEM; SU8020, HITACHI, Japan) combined with electron dispersion X-ray spectroscopy (EDS) was employed to characterize the surface morphologies and elemental compositions. The chemical states of the samples were determined by X-ray photoelectron spectroscopy (XPS; PHI 5000 VersaProbe, Ulvac-Phi, Inc.) using an AlK_a source. The binding energy values in the resulting spectra were calibrated to the C 1*s* peak at 284.8 eV.

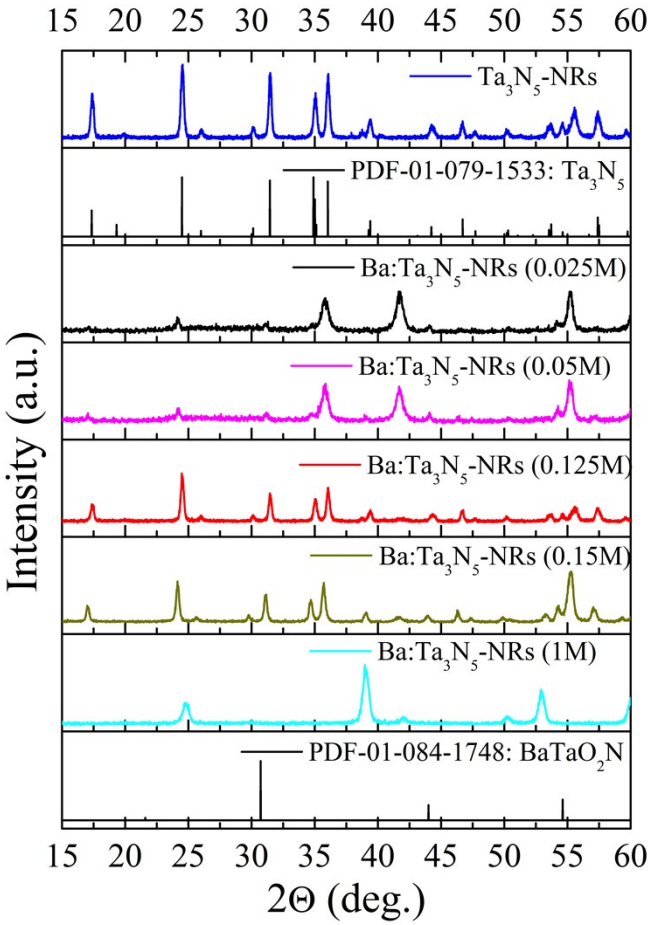

Fig. S3. X-ray diffraction patterns obtained from the Ta_3N_5-NRs and Ba:Ta_3N_5-NRs samples made with various $Ba(NO_3)_2$ precursor concentrations.

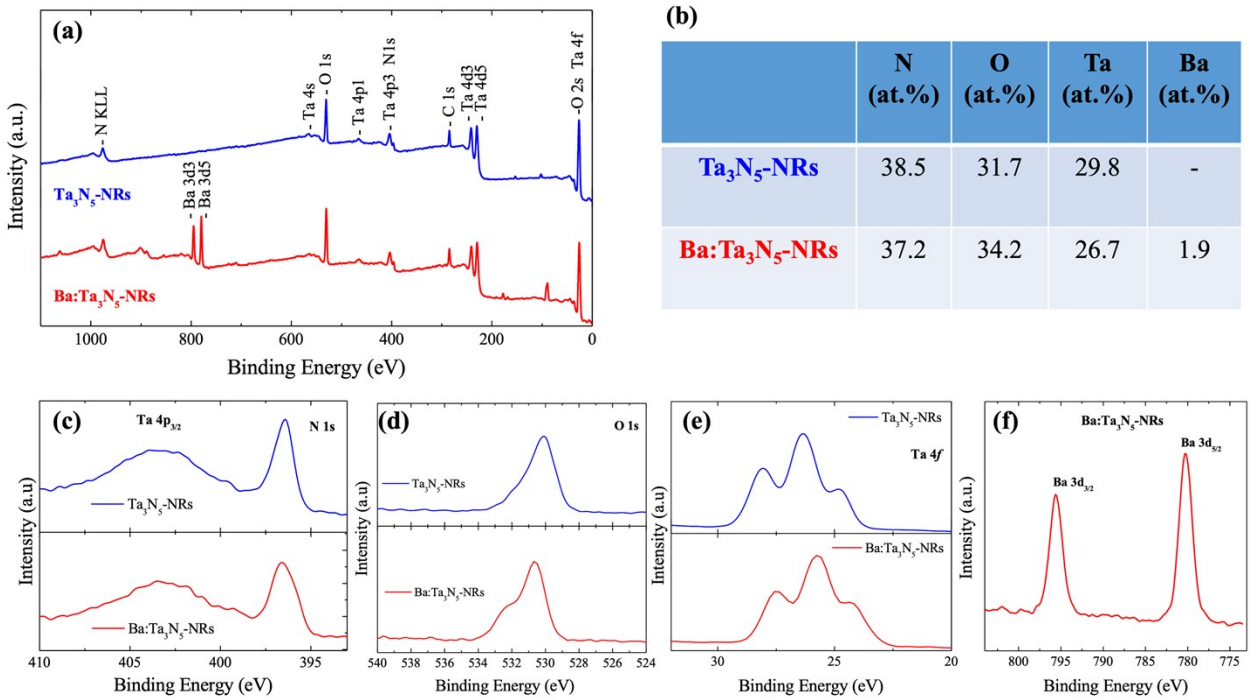

	N (at.%)	O (at.%)	Ta (at.%)	Ba (at.%)
Ta_3N_5-NRs	38.5	31.7	29.8	-
Ba:Ta_3N_5-NRs	37.2	34.2	26.7	1.9

Fig. S4. X-Ray photoelectron spectra obtained from the Ta_3N_5-NRs and Ba:Ta_3N_5-NRs. (a) Low resolution spectra. (b) Atomic concentrations of N, O, Ta and Ba estimated from the XPS data. High-resolution (c) N, (d) O, (e) Ta and (f) Ba spectra.

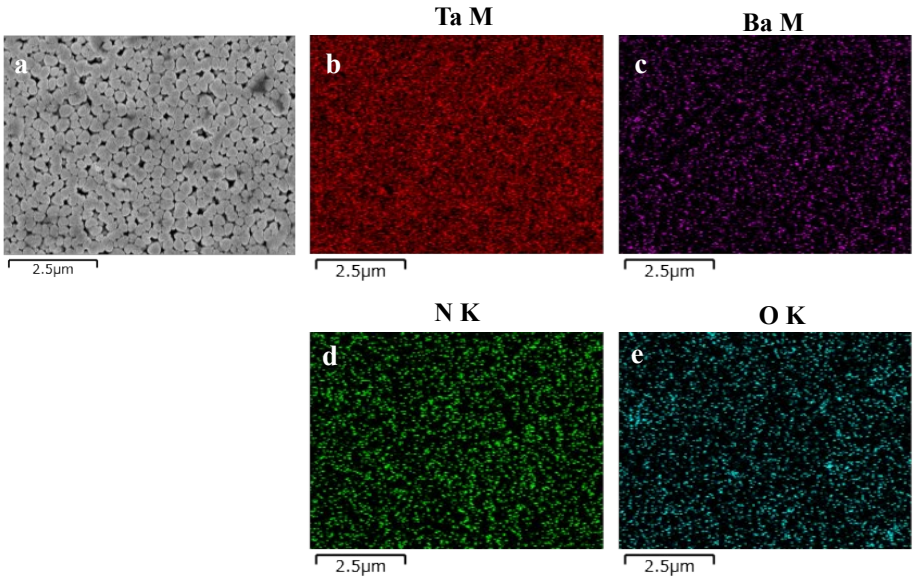

Fig. S5. EDS analyses of Ba:Ta_3N_5-NRs. (a) SEM top view image of the Ba:Ta_3N_5-NRs. (b-e) EDS elemental maps for Ta, Ba, N and O. These data confirm the uniform distribution of Ba over the Ta_3N_5-NRs surfaces.

Table S1: Elemental composition estimated from EDS mapping of the Ba:Ta_3N_5-NRs.

Element	Atomic %
Ta	42.8
N	45.1
O	11.4
Ba	0.7

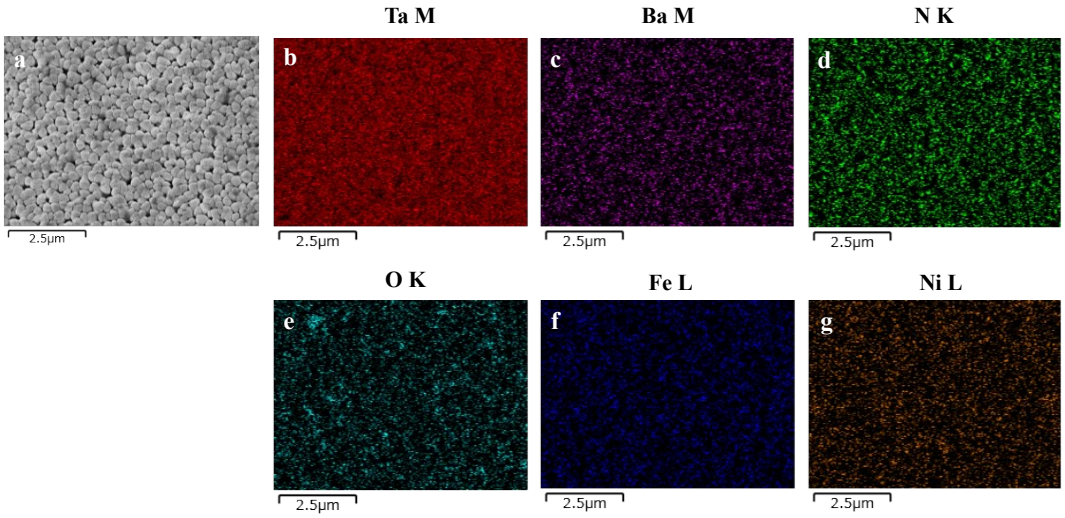

Fig. S6. EDS analyses of Ba:Ta_3N_5-NRs/$FeNiO_x$ photoanode. (a) SEM top view image of the Ba:Ta_3N_5-NRs/$FeNiO_x$ photoanode. (b-g) EDS elemental maps for Ta, Ba, N, O, Fe, and Ni. These data confirmed the uniform distributions of Fe and Ni (and therefore of the $FeNiO_x$ co-catalyst) over the Ba:Ta_3N_5-NRs surfaces.

$FeNiO_x$ co-catalyst loading Freshly made samples of Ta_3N_5-NRs and Ba:Ta_3N_5-NRs on Ta substrates with a size of 1 × 1 cm were cut in preparation for fabricating specimens homogeneously covered with the $FeNiO_x$ co-catalyst, using our previously reported protocol.[5,6] Briefly, a freshly made cocatalyst precursor solution containing 20 mM $Ni(NO_3)_2$•$6H_2O$ and 20 mM $(FeNO_3)_2$•$9H_2O$ was mixed in a ratio of 1:1 and stirred for 15 min under ambient conditions. Each specimen was immersed in the resulting solution for 10 min and then placed on a room temperature hot plate and covered with a ceramic cap. This was followed by heating of the modified sample at 55 °C in air for 15 min. Subsequently, the ceramic cap was removed and several drops of the co-catalyst precursor were applied to the sample until its surface was uniformly coated. The cap was covered again, and the loaded sample heated at 145 °C in air for 45 min, followed by rinsing with milli-Q water to remove any residual precursor and drying under a N_2 steam. Electrical contacts were fabricated on each photoanode and the specimen was encapsulated in epoxy, following which the active surface area was estimated from a photographic image using the Image-J processing program.

Characterization

Photoelectrochemical measurements As per standard photoelectrochemical (PEC) measurement protocol,[7] the PEC data were acquired in a 0.5 M K_2HPO_4 electrolyte using a three-electrode system comprising the newly fabricated photoanode (as the working electrode), a platinum counter electrode and a Ag/AgCl reference electrode. KOH was added to the electrolyte to adjust the chemical potential or pH and the electrolyte was stirred and purged with Ar gas for 15–20 min before each trial. A potentiostat (HV-100, Hokuto Denko, Japan) was used to vary the potential of the photoanode with respect to the reference electrode, $V_{Ag/AgCl}$. This potential was translated to the reversible hydrogen electrode (RHE) scale using the Nernst equation

$$V = V_{Ag/AgCl} + 0.059\text{pH} + V^{0}_{Ag/AgCl},$$

where $V^{0}_{Ag/AgCl} = 0.198\,V$ is the standard potential of Ag/AgCl at 25 °C, and V is the translated potential in RHE scale. The photoanode was irradiated using a commercial solar simulator (XES-40S2, SAN-EI Electric Co., Ltd.) calibrated to the AM1.5G level of light intensity with a solar power of 100 mW cm^{-2}. Successive potential scans were performed under chopped or continuous solar light with a scan rate of 10 mV s^{-1} to assess the stabilized current potential characteristics of the fabricated samples. The measured photocurrent was normalized relative to the photoanode active area of 0.23 – 0.25 cm^2 to obtain the current density of each material.

Incident photon to current efficiency A MAX-302 Xe light source (Asahi Spectra, Japan) with monochromatic bandpass filters was used to calculate the incident photon to current efficiency (IPCE) spectra at various wavelengths based on the equation

$$IPCE\ (\%) = \frac{hc}{q\lambda} \times \frac{J_a}{P} \times 100,$$

where, q, h, c and J_a are the electronic charge, Planck's constant, the speed of light in vacuum and the experimental current density at 1.23 V_{RHE}, respectively, *P* is the power density of the light source and λ is the irradiation wavelength.

Gas chromatography The PEC cell configuration described above was connected to both a vacuum pump and a gas chromatograph to quantify the evolution of gaseous O_2 and H_2 under the simulated

AM1.5G radiation. The vacuum pump was used to create a base pressure of several Torr, followed by the introduction of an Ar gas purge at 40 Torr to remove residual O_2 from the electrolyte.

Mott-Schottky analysis Plots were obtained from the photoanodes under dark conditions by monitoring capacitance values at various applied potentials while applying a frequency of 1000 Hz and an alternating current amplitude of 10 mV, using a VersaSTAT3 potentiostat (METEK Inc.).

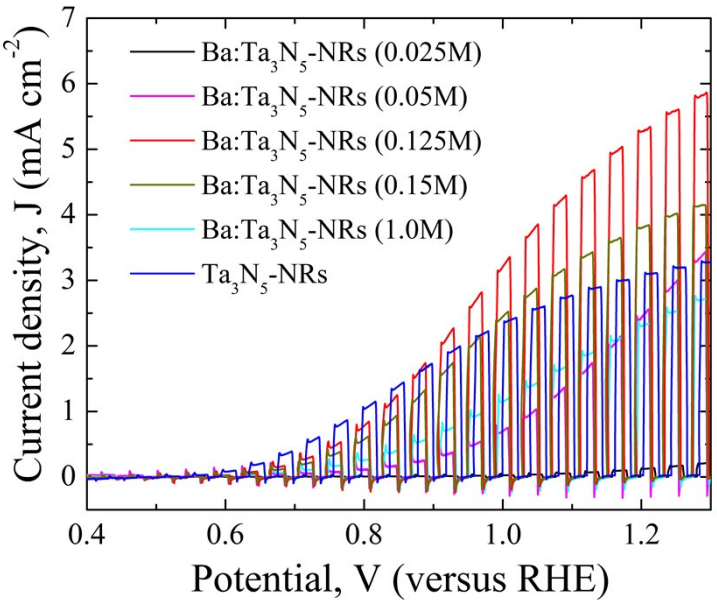

Fig. S7. Current-potential characteristics of Ta_3N_5-NRs/$FeNiO_x$ and Ba:Ta_3N_5-NRs/$FeNiO_x$ photoanodes made using various concentrations of the Ba precursor.

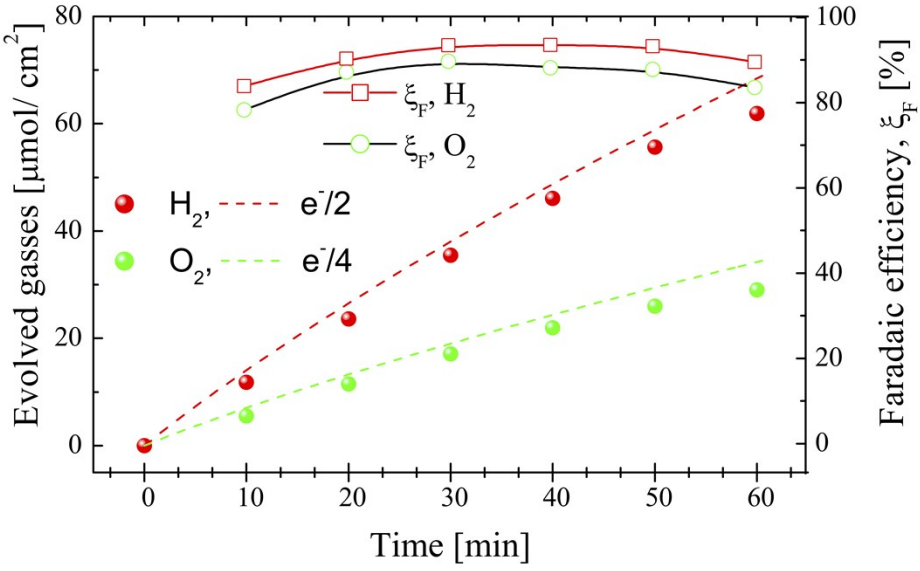

Fig. S8. Evolution of O_2 and H_2 as determined by gas chromatography along with the Faradaic efficiencies of three electrode cell configurations with Ba:Ta_3N_5-NRs/FeNiOx as working electrode at pH = 13 under simulated AM1.5G solar radiation.

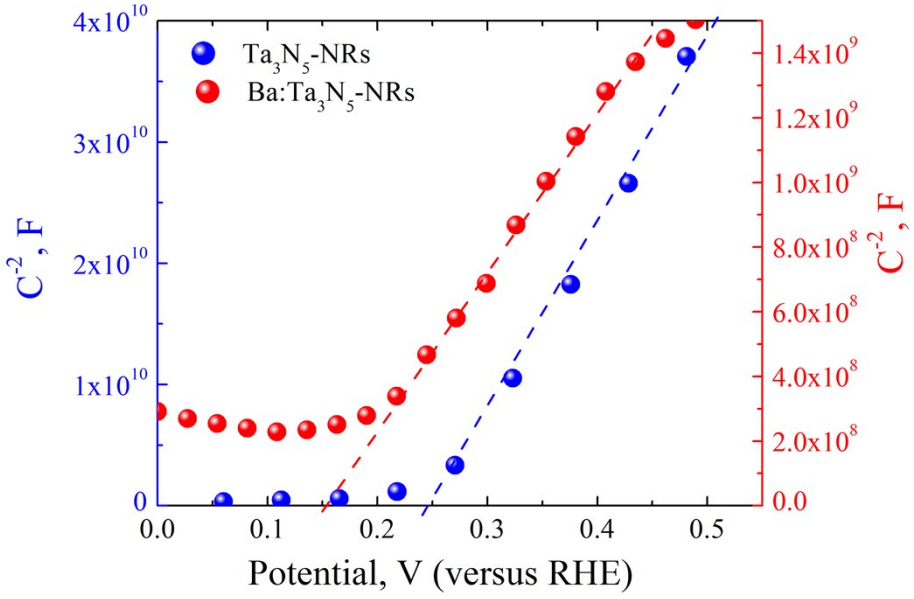

Fig. S9. Mott-Schottky plots obtained from photoanodes based on the Ta_3N_5-NRs and Ba:Ta_3N_5-NRs. The red and green dashed lines show the fitting of the linear ranges of the plots for these two materials. The intercepts of the fitting lines to the x-axis correspond to the flat band potentials, V_{FB}, for the respective photoanodes, and indicate values for the Ta_3N_5-NRs and Ba:Ta_3N_5-NRs photoanodes of 0.25 and 0.16

V_{RHE}, respectively. The carrier concentration, N_D, was determined for both photoanodes using the equation

$$N_D=2/(\varepsilon\varepsilon_o e k_{MS} f_r^2),$$

where ε is the dielectric constant of Ta_3N_5, ε_o is the permittivity of a vacuum, e is the electron charge, k_{MS} is the slope of the Mott-Schottky fitting line, and f_r is the roughness factor of the Ta_3N_5-NRs. The f_r values for both samples were estimated using the Image J processing software based on overhead view and cross-sectional SEM images of both photoanodes. These values were approximately 9.9 and 10.5 for the Ta_3N_5-NRs and Ba:Ta_3N_5-NRs.

Methodology for simulations

Optical Simulations Optical simulations were performed to quantify light absorption in addition to optical losses such as transmission and reflection for the Ta_3N_5-NRs photoanodes. These simulations assumed linearly polarized light with a power of 1 W incident perpendicular to a glass (200 nm)/water (200 nm)/non-uniform or uniform cylindrical Ta_3N_5-NRs/substrate specimen. The model used average dimensions, shapes and periodicity for the Ta_3N_5-NRs, as shown in Fig. S10(a), based on SEM images of the actual samples fabricated in this work. The refractive index, n_r, and extinction coefficient, k_e, used for Ta_3N_5 in the optical calculations are provided in Fig. S10(b).[6] Values of n_r = *1.47*, *1.33* and *3* were employed for glass, water and the substrate, respectively. Because the Ta_3N_5-NRs was the only light-absorbing medium, k_e = *0* for each layer except NRs. The model photoanode comprised a uniform coating of NRs on a substrate with a specific average periodicity across its cross-sectional area, and so continuous periodic boundary conditions for electric field were applied to the opposite faces to capture the effects of light trapping and scattering. The COMSOL Multiphysics optics module was employed to solve Maxwell equations for electromagnetic waves at each discretised node related to the propagation of the electric field of polarized light at various wavelengths, λ. The phase elimination method[8] was utilized to simulate optical losses and light absorption of the modelled device, which are plotted against λ in Fig. 3 for non-uniform NRs and in Fig. 4 for uniform Ta_3N_5-NRs (as described in the main text). To reduce computational complexity, a modified Beer-Lambert law was used to determine the rate, *G(z)*, at which charge carriers were generated in response to the absorption of simulated light, $Abs(\lambda)$, for a given photon flux density with AM1.5G solar radiation, $N(\lambda)$ (see Fig. S10(c)). The associated equation

was $G(z) = \int N(\lambda)Abs(\lambda)[\alpha(\lambda)/(1 - \exp(-\alpha(\lambda)L))]\exp(-\alpha(\lambda)z)d\lambda$, in which the term $1 - \exp(-\alpha(\lambda)L)$ in the denominator takes into account absorption along the finite length of the NRs.

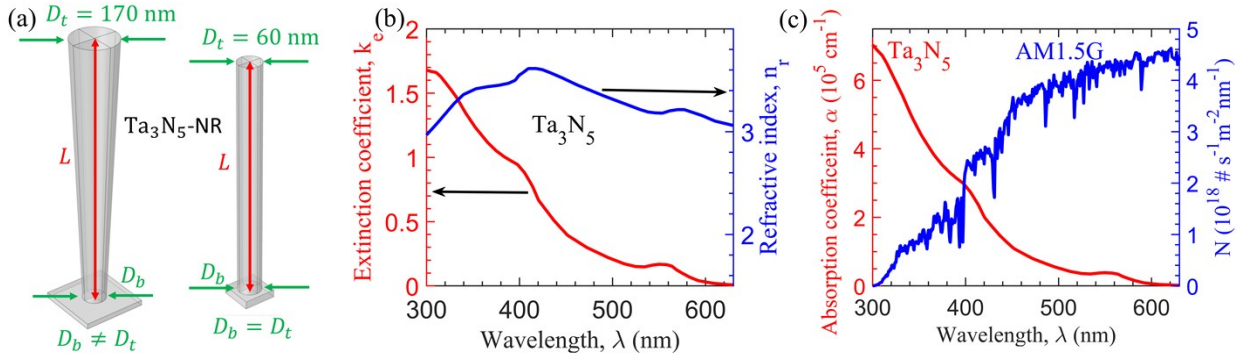

Fig. S10. (a) A diagram of the model for a cylindrical Ta_3N_5-NRs photoanode with non-uniform (D_b=D_t/2) and uniform (D_b=D_t) diameter and length, *L*. (b) The refractive index, n_r, and extinction coefficient, k_e, of Ta_3N_5 as functions of wavelength.[6] (c) The calculated photon flux density, *N*, of the AM1.5G solar spectrum at an intensity of 100 mW cm^{-2} and the absorption coefficient, $\alpha = 4\pi k_e/\lambda$, as functions of wavelength, λ.

Electrical simulations Electrical simulations were performed to investigate various performance-limiting parameters and quantify electrical losses due to factors such as recombination and resistivity for both the present Ba:Ta_3N_5-NRs and Ta_3N_5-NRs photoanodes as well as those previously reported in the literature. For this purpose, both non-uniform and uniform Ta_3N_5-NRs (based on SEM images) interfaced with substrates were employed as model systems, Fig. S10(a). The charge carriers in this simulation were produced at the rate, *G(z)*, previously estimated from the optical simulations. Recombination of photogenerated charge carriers *R* was assumed to occur *via.* a trap-assisted Shockley-Read-Hall process (characterized by a carrier lifetime, τ) and bi-molecular radiative recombination (with a rate coefficient, k_r).[9] The electrolyte and co-catalyst for the oxygen evolution reaction at the NRs surfaces were modelled using effective pseudo Schottky contacts with a work function, W_{el}, and a non-zero hole extraction rate or surface recombination velocity for holes, S_h. In addition, Ohmic contact was assumed at the substrate. Due to the non-trivial charging or pinning effects, the value of W_{el} was set according to the estimated flat band potential obtained from the Mott-Schottky plots for the respective samples. Additional details of the material parameters are provided in Table S2. The semiconductor module of the COMSOL Multiphysics program was used to carry out these electrical simulations by determining a self-consistent solution to Poisson's equation, as well as the drift-diffusion and continuity equations for electrons and

holes at each discretised node. Figs. 3(d) and (e) in the main text show the results of respective quantities along one-dimensional across NR diameter at 200 nm from the NR top. The effect of series resistance, R_s, was included by adjusting the potential axis with V_s+JR_s, where V_s was the potential on ohmic substrate in the RHE scale and J was the simulated photocurrent density.

Table S2. Material parameters employed for electrical simulations of Ta_3N_5-NRs and Ba:Ta_3N_5-NRs photoanodes based on the present samples and photoanodes previously reported in the literature.

Parameters	Fabricated samples (Fig. 3)	Reported samples (Fig. 4)
Geometry	Non-uniform cylindrical NRs[a]	Uniform cylindrical NRs[a]
NR diameter at top D_t and bottom D_b	D_t=170 nm, D_b=65 nm[a]	D_t=D_b=60 nm[a,10]
Length of NR, L	1000 nm[a]	600 nm[a]
Electron affinity	3.92 eV [11]	3.92 eV [11]
Energy band gap E_g	2.1 eV [11]	2.1 eV [11]
Dielectric constant, ϵ	17 [12]	17 [12]
Effective density of states for conduction band N_c and valence band N_v	10^{20} cm^{-3} [6]	10^{20} cm^{-3} [6]
Carrier mobility μ	1.3 $cm^2/V\,s$ [12]	1.3 $cm^2/V\,s$ [12]
Bi-molecular recombination rate coefficient, k_r	10^{-11} $cm^3\,s^{-1}$ [b]	10^{-11} $cm^3\,s^{-1}$ [b]
SRH carrier lifetime τ	1 ps – 1µs [c]	1 ps – 1µs [c]
n-type doping density, N_D	1.06×10^{18} cm^{-3} – Ta_3N_5[d] 2.83×10^{19} cm^{-3} – Ba:Ta_3N_5[d]	3.7×10^{19} cm^{-3} – Ta_3N_5[d, 10] 5.8×10^{19} cm^{-3} – Ba:Ta_3N_5[d, 10]
Electrolyte Work function at NR surface, W_{el}	4.28 eV – Ta_3N_5[d] 4.37 eV – Ba:Ta_3N_5[d]	4.38 eV – Ta_3N_5[d, 10] 4.48 eV – Ba:Ta_3N_5[d, 10]
Back contact	Ohmic	Ohmic

[a] As determined from SEM images of the samples.

[b] Typical values for direct band gap photo-absorbing semiconductor materials.

[c] Variable parameter for calibration of the model based on experimental photocurrent density data obtained at 1.23 V_{RHE} for the respective photoanodes.

[d] Estimated parameters obtained from experimental Mott-Schottky plots for undoped Ta_3N_5-NRs and Ba:Ta_3N_5-NRs photoanodes.

Table S3. Estimated values of various parameters obtained from the calibration of the simulation with experimental data for Ba:Ta_3N_5-NRs and Ta_3N_5-NRs photoanodes.

Parameters	For fabricated samples		For reported samples	
	Ba:Ta_3N_5-NRs	Ta_3N_5-NRs	Ba:Ta_3N_5-NRs	Ta_3N_5-NRs
Carrier Lifetime τ	0.25 ns	3 ps	0.3 ns	50 ps
Effective lifetime τ_{eff}	0.23 ns	3 ps	0.25 ns	49 ps
Diffusion length L_D	27.88 nm	3.18 nm	29 nm	12.8 nm
Resistance R_s	50 Ω cm^2	70 Ω cm^2	20 Ω cm^2	50 Ω cm^2
Hole extraction rate S_h	10^{-5} cm s^{-1}	2.5×10^{-3} cm s^{-1}	10^{-6} cm s^{-1}	3.5×10^{-3} cm s^{-1}

Table S4. Summary of various GLAD and nitridation parameters employed for the fabrication of Ta_3N_5-NRs using a non-optimized Ar plasma and an optimized mixed plasma.

Main GLAD parameters		
	Non-optimized	Optimized
Working gas(es) and flow rate (sccm)	Ar, 15	Ar/N_2 15/10
Working pressure (Pa)	0.38	1.3
Magnetron power (W)	300	250
GLAD angle- α (deg.)	85	86
Sample rotation speed- φ (rpm.)	45	90
Nitridation parameters		
Flow rate of NH_3 (sccm)	250	50
Temperature (°C) and ramping rate (°C/min)	980 8	980 8
Time (min)	150	150
Cooling to 25°C	Natural in NH_3 (at 250 sccm)	Natural in NH_3 (at 50 sccm)
Removing residual NH_3 by N_2 (at flow rate 250 sccm) within 15 min		

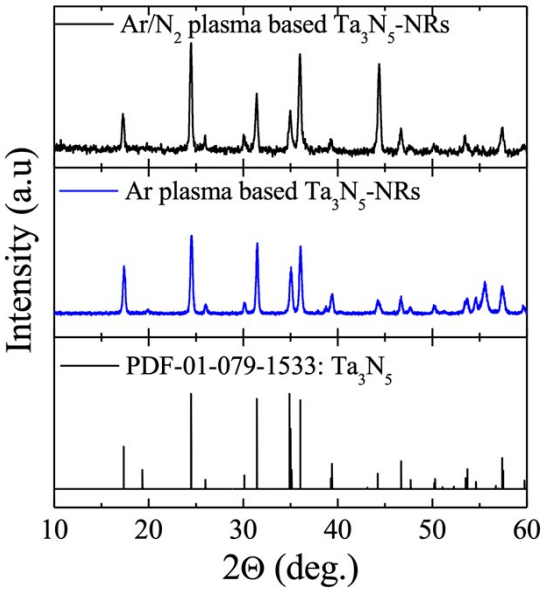

Fig. S11. XRD patterns of Ta_3N_5-NRs specimens prepared from the nitridation of TaN_x-NRs made using (a) a mixed Ar/N_2 plasma and (b) an Ar plasma. The reference pattern for Ta_3N_5 (PDF-01-079-1533) is also included.

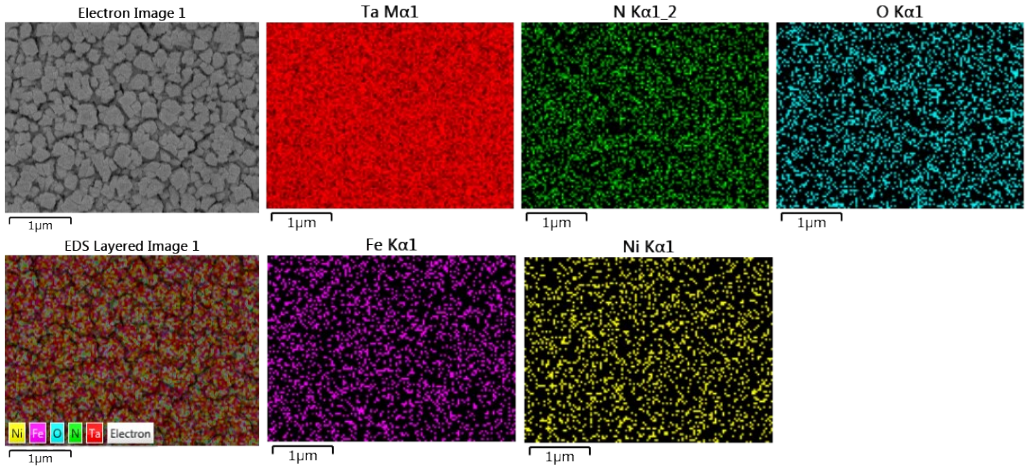

Fig. S12. EDS analyses of the Ta_3N_5-NRs/$FeNiO_x$ prepared from TaNx-NRs using a mixed Ar/N_2 plasma (after nitridation). The figure shows a top view SEM image of the photoanode along with EDS elemental maps for Ta, N, O, Fe and Ni that confirm the uniform distribution of the various elements on the surface.

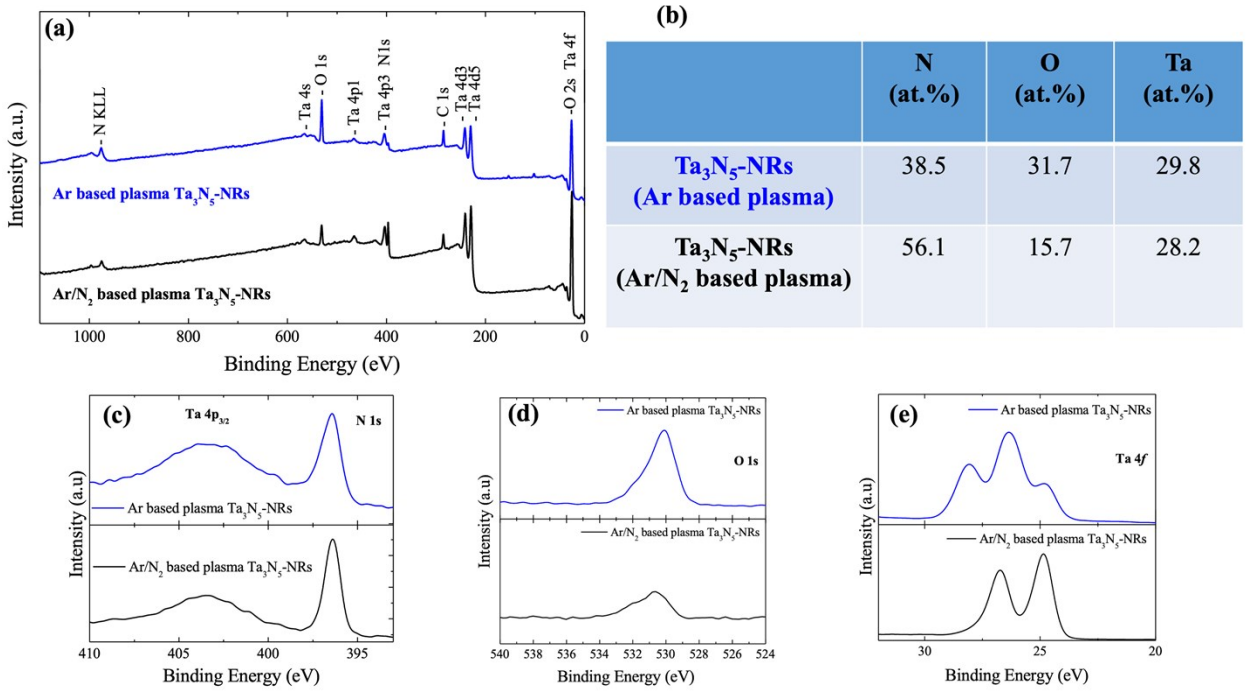

	N (at.%)	O (at.%)	Ta (at.%)
Ta_3N_5-NRs (Ar based plasma)	38.5	31.7	29.8
Ta_3N_5-NRs (Ar/N_2 based plasma)	56.1	15.7	28.2

Fig. S13. Data obtained from Ta_3N_5-NRs made using a mixed Ar/N_2 plasma followed by nitridation. (a) Low resolution XPS spectra, (b) atomic concentrations of N, O and Ta obtained from the XPS analysis, and (c), (d) and (e) high resolution N, O and Ta spectra, respectively.

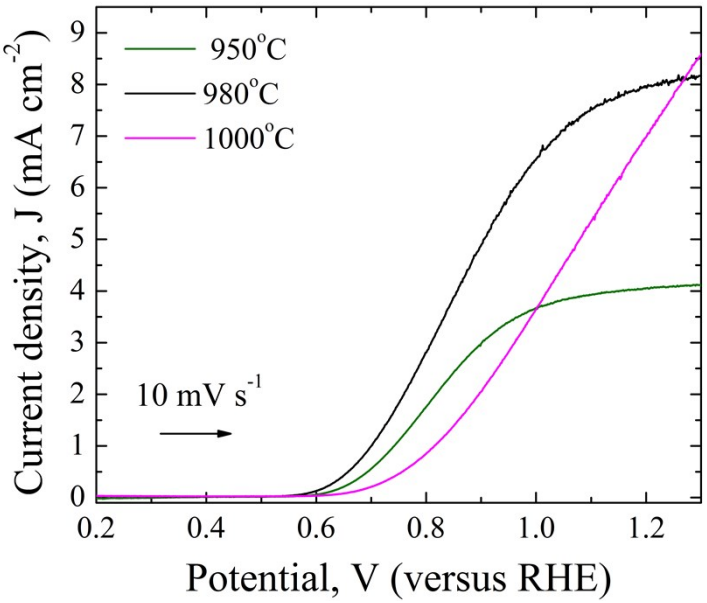

Fig. S14. Current-potential characteristics of Ta_3N_5-NRs/FeNiOx photoanodes prepared from the TaNx-NRs made using a mixed Ar/N_2 plasma and nitridated at various temperatures.

References

1 K. Robbie and M. J. Brett, *J. Vac. Sci. Technol. A*, 1997, **15**, 1460–1465.

2 Y. Pihosh, I. Turkevych, K. Mawatari, N. Fukuda, R. Ohta, M. Tosa, K. Shimamura, E. G. Villora and T. Kitamori, *Nanotechnology*, 2014, **25**, 315402.

3 Y. Pihosh, I. Turkevych, K. Mawatari, T. Asai, T. Hisatomi, J. Uemura, M. Tosa, K. Shimamura, J. Kubota, K. Domen and T. Kitamori, *Small*, 2014, **10**, 3692–3699.

4 Y. Pihosh, I. Turkevych, K. Mawatari, J. Uemura, Y. Kazoe, S. Kosar, K. Makita, T. Sugaya, T. Matsui, D. Fujita, M. Tosa, M. Kondo and T. Kitamori, *Sci. Rep.*, 2015, **5**, 11141.

5 Y. Pihosh, T. Minegishi, V. Nandal, T. Higashi, M. Katayama, T. Yamada, Y. Sasaki, K. Seki, Y. Suzuki, M. Nakabayashi, M. Sugiyama and K. Domen, *Energy Environ. Sci.*, 2020, **13**, 1519–1530.

6 Y. Pihosh, V. Nandal, T. Minegishi, M. Katayama, T. Yamada, K. Seki, M. Sugiyama and K. Domen, *ACS Energy Lett.*, 2020, **5**, 2492–2497.

7 Z. Chen, T. F. Jaramillo, T. G. Deutsch, A. Kleiman-Shwarsctein, A. J. Forman, N. Gaillard, R. Garland, K. Takanabe, C. Heske, M. Sunkara, E. W. McFarland, K. Domen, E. L. Miller, J. A. Turner and H. N. Dinh, *J. Mater. Res.*, 2010, **25**, 3–16.

8 A. Campa, J. Krc and M. Topic, *Prog. Electromagn. Res.*, 2013, **137**, 187–202.

9 R. F. Pierret, *Semiconductor Device Fundamentals*, Addison-Wesley, 1996.

10 Y. Li, L. Zhang, A. Torres-Pardo, J. M. González-Calbet, Y. Ma, P. Oleynikov, O. Terasaki, S. Asahina, M. Shima, D. Cha, L. Zhao, K. Takanabe, J. Kubota and K. Domen, *Nat. Commun.*, 2013, **4**, 2566.

11 W.J. Chun, A. Ishikawa, H. Fujisawa, T. Takata, J. N. Kondo, M. Hara, M. Kawai, Y. Matsumoto and K. Domen, *J. Phys. Chem. B*, 2003, **107**, 1798–1803.

12 A. Ziani, E. Nurlaela, D. S. Dhawale, D. A. Silva, E. Alarousu, O. F. Mohammed and K. Takanabe, *Phys. Chem. Chem. Phys.*, 2015, **17**, 2670–2677.